Cancer Immunology, Immunotherapy (2025) 74:123
https://doi.org/10.1007/s00262-025-03968-7

RESEARCH

Spatial transcriptomics reveals prognostically *LYZ*+ fibroblasts and colocalization with *FN1*+ macrophages in diffuse large B-cell lymphoma

Liyuan Dai[1] · **Ning Lou**[1,3] · **Liling Huang**[1] · **Lin Li**[2] · **Le Tang**[1] · **Yuankai Shi**[1] · **Xiaohong Han**[3]

Received: 21 November 2024 / Accepted: 2 February 2025 / Published online: 25 February 2025

Abstract

Background Diffuse large B-cell lymphoma (DLBCL) is a clinically heterogeneous malignancy with diverse patient outcomes, largely influenced by the tumor microenvironment (TME). Understanding the roles of fibroblasts and macrophages within the TME is essential for developing personalized therapeutic strategies in DLBCL.
Methods This study is a multi-omics approach, integrating spatial transcriptomics ($n = 11$), bulk transcriptomics ($n = 2{,}499$), immunohistochemistry (IHC, $n = 37$), multiplex immunofluorescence (mIF, $n = 56$), and plasma samples ($n = 240$) to identify and characterize fibroblast and tumor-associated macrophage subtypes in the TME. Hub genes for *LYZ*+ fibroblasts and *FN1*+ macrophages were selected through univariate Cox regression and random forest analyses. Their prognostic significance was validated using IHC, mIF, and autoantibody assays in DLBCL patients treated with R-CHOP and in non-small cell lung cancer (NSCLC) patients receiving immune checkpoint inhibitors (ICIs).
Results Fibroblasts and macrophages were classified into two distinct subtypes. Patients with higher *LYZ*+ fibroblasts infiltration demonstrated superior prognosis, which was associated with increased infiltration of *FN1*+ macrophages. Key hub genes identified for *LYZ*+ fibroblasts included *LYZ, ANPEP, CSF3R, C15orf48, LILRB4, CLEC7A,* and *COL7A1*, while hub *FN1*+ macrophages genes included *COL1A1, FN1, APOE, DCN, MMP2, SPP1, COL3A1,* and *COL1A2*. Independent prognostic markers in DLBCL treated with R-CHOP and NSCLC treated with ICIs were identified, including LYZ and LILRB4 at both protein and mRNA levels, and COL1A2 autoantibodies ($p < 0.05$). In DLBCL patients treated with R-CHOP, *FN1* mRNA and autoantibody levels were also prognostic markers ($p < 0.05$). In NSCLC treated with ICIs, COL3A1 autoantibody was prognostic marker ($p < 0.05$).
Conclusions This study identified a prognostically relevant *LYZ*+ fibroblasts and *FN1*+ macrophages in DLBCL. The hub genes associated with these subtypes represent potential biomarkers, providing insights into improving patient outcomes in DLBCL.

Keywords Spatial transcriptomics · Diffuse large B cell lymphoma · Cancer-associated fibroblasts · Tumor-associated macrophages · Prognostic marker

Introduction

Diffuse large B-cell lymphoma (DLBCL) is the most prevalent and clinically heterogeneous subtype of non-Hodgkin lymphoma, accounting for approximately 30–40% of cases globally [1]. Despite significant advances in therapeutic strategies, including immunochemotherapy regimens such as R-CHOP (rituximab, cyclophosphamide, doxorubicin, vincristine, and prednisone), a substantial proportion (20–50%) of DLBCL patients exhibit resistance to treatment or relapse, leading to poor prognostic outcomes [2]. While conventional clinical prognostic tools, such as the International Prognostic Index, provide valuable risk stratification, they do not account for key cellular interactions within the tumor microenvironment (TME) that can impact patient outcomes [3]. This clinical variability underscores the necessity for a deeper understanding of the TME and its contribution to disease progression, treatment response, and patient survival. The TME consists of a complex network of tumor cells,

---

Liyuan Dai, Ning Lou and Liling Huang are co-first authors and contributed equally to this work.

Extended author information available on the last page of the article

stromal cells, and infiltrating immune cells, including fibroblasts and macrophages, which play critical roles in tumor progression and immune evasion [4]. Recent studies have highlighted the importance of understanding the cellular and molecular composition of the TME for the development of more effective, personalized treatment strategies in DLBCL [5]. In particular, the roles of tumor-associated macrophages (TAMs) and cancer-associated fibroblasts (CAFs) in modulating the immune response and promoting tumor growth have garnered increasing attention.

Although fibroblasts were initially regarded as ‘immune-neutral’ structural determinants, studies have shown that they play a key role in regulating immune cells and influencing responses to immunotherapy [6]. Stromal-immune crosstalk is highly relevant in the era of immunotherapy. The effectiveness of immunotherapy in different types of lymphoma has shown promise, with Hodgkin lymphoma being classified as a ‘hot’ tumor containing a relatively large number of tumor-infiltrating lymphocytes that respond well to programmed cell death protein 1 blockade. However, most non-Hodgkin lymphomas, including DLBCL, currently fall into the unclear categories of ‘immunosuppressive’ and ‘cold’ TME, leading to poor responses to anti-PD-1 immunotherapy [7, 8]. Fibroblasts in the TME may exhibit both tumor-promoting and anti-tumor phenotypes [9, 10]. Transcriptomic studies of DLBCL tissues have elucidated the relationship between the stromal and immune cell landscape in lymphoma, capturing clinical heterogeneity beyond cell of origin and genotype classification [11, 12]. A gene signature closely associated with fibroblasts has been demonstrated to correlate with favorable survival rates in DLBCL [13], and the prognostic predictive role of fibroblasts has also been reported in follicular lymphoma [14] and Hodgkin’s lymphoma [15]. However, a comprehensive characterization of fibroblast and macrophage subtypes in DLBCL, particularly in relation to their prognostic significance and potential as therapeutic targets, remains lacking. In our previous study [16], we characterized the heterogeneity of TAMs and high glycolysis B cells in DLBCL, identifying a specific TAM cluster associated with poor prognosis and an exhausted immune microenvironment. Building on these findings, the current study shifts the focus to fibroblast heterogeneity, particularly *LYZ*$^+$ fibroblasts, and their interactions with *FN1*$^+$ macrophages. This approach provides new insights into the stromal-immune crosstalk within the DLBCL TME and its impact on patient outcomes.

In this study, we utilized a multi-omics approach, integrating spatial transcriptomics, bulk transcriptomics, immunohistochemistry, and multiplex immunofluorescence to systematically explore the fibroblast and macrophage subtypes in the DLBCL TME. By identifying key hub genes and validating their prognostic value, we aim to provide new insights into the cellular dynamics of the TME and to uncover potential biomarkers for improving patient stratification and treatment outcomes.

Methods

Reagents and tools table

Reagent/resource	Reference or source	Catalog number
Spatial transcriptomics		
Formalin-fixed paraffin-embedded samples	CHCAMS	[16]
Hematoxylin	S330930-2	Dako
Eosin	HT110216	Sigma-Aldrich
Glycerol	15514011	Thermo Fisher
HCl	H1758	Sigma-Aldrich
Visium spatial gene expression for FFPE reagent kit	1000338 (Human transcriptome)	10×Genomics
Spatial TME database	http://labwebsite.yelab.site:1234/#!/	N/A
Single-cell RNA sequencing		
Single-cell RNA sequencing samples	GSE182434	[12]
CellMarker	http://biocc.hrbmu.edu.cn/CellMarker/	N/A
Panglao DB	https://panglaodb.se/	N/A
Bulk-RNA sequencing		
Gene expression omnibus (GEO)	http://www.ncbi.nlm.nih.gov/geo	N/A
RNA sequencing samples receiving R-CHOP	GSE31312	[17]
	GSE181063	[18]
	GSE136971	[19]
RNA sequencing samples receiving immunotherapy	GSE100797 (CAR-T)	N/A
	GSE126044 (Anti-PD-1/PD-L1)	N/A
	GSE173839 (Anti-PD-L1)	N/A
	GSE91061 (Anti-PD-1/CTLA-4)	N/A
	GSE35640 (Anti-MAGE-A3)	N/A
	GSE176307	N/A
	GSE165278, GSE78220, GSE91061	N/A

Reagent/resource	Reference or source	Catalog number
KM Plot database	https://kmplot.com/analysis/	N/A
Metascape website	https://metascape.org/gp/index.html	N/A
String website	https://cn.string-db.org/	N/A
Biomarker exploration of solid tumors	https://rookieutopia.hiplot.com.cn/app_direct/BEST/	N/A
Plasma proteomics antigen microarray		
Plasma samples of DLBCL	CHCAMS	[20, 21]
Plasma samples of aNSCLC	CHCAMS	[22]
Plasma samples of healthy control	CHCAMS	[21]
HuProt$^{\text{TM}}$ human proteome high-density antigen microarray	CDI Labs	Version 3.1
Bovine serum albumin (BSA)	9048–46-8	Sigma
Alexa fluor 647 goat anti-human IgG	109–605-003	Jackson
Immunohistochemistry		
Formalin-fixed paraffin-embedded samples of DLBCL	CHCAMS	N/A
Formalin-fixed paraffin-embedded samples of aNSCLC	CHCAMS	N/A
Rabbit anti-human LYZ IgG antibody	ab108508	Abcam
Rabbit anti-human LILRB4 IgG antibody	#55107	Signalway antibody
HRP-labeled goat anti-rabbit IgG secondary antibody	GB23303	Servicebio
hematoxylin	G1004	Servicebio
Microscope	Nikon	E100
CaseViewer 2.4	3DHISTECH	Hungary
Multiple Immunofluorescence		
Formalin-fixed paraffin-embedded samples	CHCAMS	N/A
Rabbit anti-human LYZ IgG antibody	ab108508	Abcam
Rabbit anti-human LILRB4 IgG antibody	#55107	Signalway antibody
Mouse anti-human pan Cytokeratin IgG antibody	GB122053	Servicebio
HRP-labeled goat anti-rabbit IgG secondary antibody	GB23303	Servicebio
HRP-labeled goat anti-mouse IgG secondary antibody	GB23301	Servicebio
DAPI	G1012	Servicebio
Microscope	Nikon	ECLIPSE C1
Rabbit anti-human COL1A2 IgG antibody	sc-393573	Santa Cruz Biotechnology
Rabbit anti-human COL3A1 IgG antibody	#63034S	Cell Signaling Technology
Rabbit anti-human FN1 IgG antibody	#26836S	Cell Signaling Technology
Rabbit anti-human CD68 IgG antibody	ab303565	Abcam
Scanner	3DHISTECH	Pannoramic MIDI
CaseViewer 2.4	3DHISTECH	Hungary
ImageJ	https://imagej.net/software/imagej/	N/A
Software		
NovaSeq 6000	https://www.illumina.com.cn/systems/sequencing-platforms/novaseq.html	Illumina
R(4.3.1)	https://www.R-project.org/	N/A
Sanger plot website	http://www.sangerbox.com	N/A
Hiplot website	https://hiplot.com.cn/home/index.html	N/A
GenePix 4300A microarray scanner	Molecular Devices	141,095
GenePix Pro v.6.0	Molecular Devices	N/A

All the materials and tools in this study were listed in the Reagents and tools table.

DLBCL and aNSCLC sample collection

47 formalin-fixed paraffin-embedded (FFPE) and 125 plasma samples from DLBCL patients were retrospectively collected before first-line R-CHOP treatment at the Cancer Hospital, Chinese Academy of Medical Sciences (CHCAMS), between 2010 and 2023. These samples were used for spatial transcriptomics (ST), immunohistochemistry (IHC), multiple immunofluorescence (mIF), and plasma proteomics. Specifically, samples from 2019 to 2023 were used for ST, while those collected from 2010 to 2020 were used for IHC, mIF, and proteomics. All plasma samples [20, 21] were collected using ethylenediaminetetraacetic acid, centrifuged at 867 rcf and 4 °C for 10 min, and stored in 2 ml conical tubes at −80 °C until the microarray assay. FFPE samples were stored at room temperature. Additionally, one lymph node ST sample was obtained from the Spatial TME database (http://labwebsite.yelab.site:1234/#!/). Inclusion criteria consisted of DLBCL patients with available samples obtained prior to first-line R-CHOP chemotherapy, who had undergone at least two cycles of R-CHOP and had complete clinical data. Exclusion criteria encompassed patients with secondary primary cancers, primary central nervous system DLBCL, or DLBCL that transformed from indolent lymphoma. The efficacy of R-CHOP was evaluated using the 2014 Lugano criteria. In total, 47 DLBCL patients were included across two cohorts: ST ($n=10$) [16], IHC ($n=37$), and mIF ($n=27$). Six out of ten patients in the ST cohort and all patients in the IHC cohorts were followed up for more than two years.

Between 2016 and 2022, a total of 36 [22] pretreatment plasma samples were obtained and 29 FFPE samples from 65 advanced non-small cell lung cancer (aNSCLC) patients who received immune checkpoint inhibitors (ICIs) therapy (nivolumab, pembrolizumab, sintilimab, triplimab, camrelizumab, or tirellizumab) at the CHCAMS. These samples were used for mIF and plasma proteomics. The inclusion criteria for patients were: (1) biopsy-confirmed aNSCLC and complete clinical follow-up data; (2) aNSCLC patients receiving ICIs therapy; and (3) use of ICIs as first-line or later-line treatment. aNSCLC patients meeting any of these conditions were excluded: (1) with other concurrent cancers; (2) with non-primary lung tumors; (3) having concomitant autoimmune diseases; and (4) using other immunosuppressive agents (e.g., steroid medication). The efficacy of immunotherapy was evaluated using Response Evaluation Criteria in Solid Tumors (RECIST) version 1.1. Detailed patient characteristics are provided in Tables S1 and S2, and the study flowchart is shown in Fig. 1. This study was approved by the Ethics Committee of the National Cancer Center/National Clinical Research Center for Cancer/Cancer Hospital, Chinese Academy of Medical Sciences & Peking Union Medical College (No. 23/262-4004). All experiments were conducted in accordance with the Declaration of Helsinki.

For scRNA-seq, data from GSE182434 [12], which encompassed four tumor samples from DLBCL patients, were retrieved. Clinical data and metadata were obtained from the original study [12]. For bulk RNA-seq, data were extracted from three GEO datasets (http://www.ncbi.nlm.nih.gov/geo): GSE31212 ($n=470$) [17], GSE181063 ($n=802$) [18], and GSE136971 ($n=109$) [19]. They were collected from tissue samples prior to R-CHOP treatment, with accompanying survival data.

Spatial transcriptomics analysis of cancer-associated fibroblasts and macrophages

For the 10 ST samples, the experimental procedures, data preprocessing, sample integration, CARD deconvolution, cell type annotation, and intratumoral heterogeneity score analysis were performed as same as described in our original study [16].

First, we performed clustering and dimensionality reduction for fibroblast cells. After data preprocessing and integration, distinct subclusters of fibroblast cells and macrophages were isolated. The data were segmented using the 'FindClusters' function with a resolution of 0.15 for fibroblast cells and 0.3 for macrophages. The 'RunUMAP' function was used to create a two-dimensional representation of the first 30 principal components through uniform manifold approximation and projection (UMAP). Marker genes for each cell type were identified with the 'FindAllMarkers' function, selecting genes detected in at least 25% of cells within the cluster, with a p value <0.05 from the Wilcoxon test and a differential expression threshold of 0.25 log fold change (log FC). Visualization of differentially expressed genes was performed using DotPlot, VlnPlot, and DoHeatmap functions.

Next, we analyzed cell metabolic activity, gene set functional enrichment, and transcription factor activity in fibroblast cell types. The 'scMetabolism' package, designed for quantifying single-cell metabolism, systematically evaluated and scored clusters within 79 individual metabolic pathways from conventional single-cell matrix files using a vision algorithm. Gene set enrichment analysis (GSEA) was performed using the irGSEA tool. Transcription factor (TF) activity was inferred with the DoRothEA package, selecting high-confidence TFs ('A', 'B', and 'C') based on 'dorothea_hs' regulons provided by the package. Viper scores were calculated, scaled, and integrated into the Seurat object as the 'Dorothea' attribute. To facilitate comparison of TF activity, mean and standard deviation were computed for scaled Viper scores within each cell type, and TFs were ranked based on the variance of their Viper scores. The top 20 TFs with the most variable scores in each cell type were selected for visualization. The 'Cellchat' package was used to explore

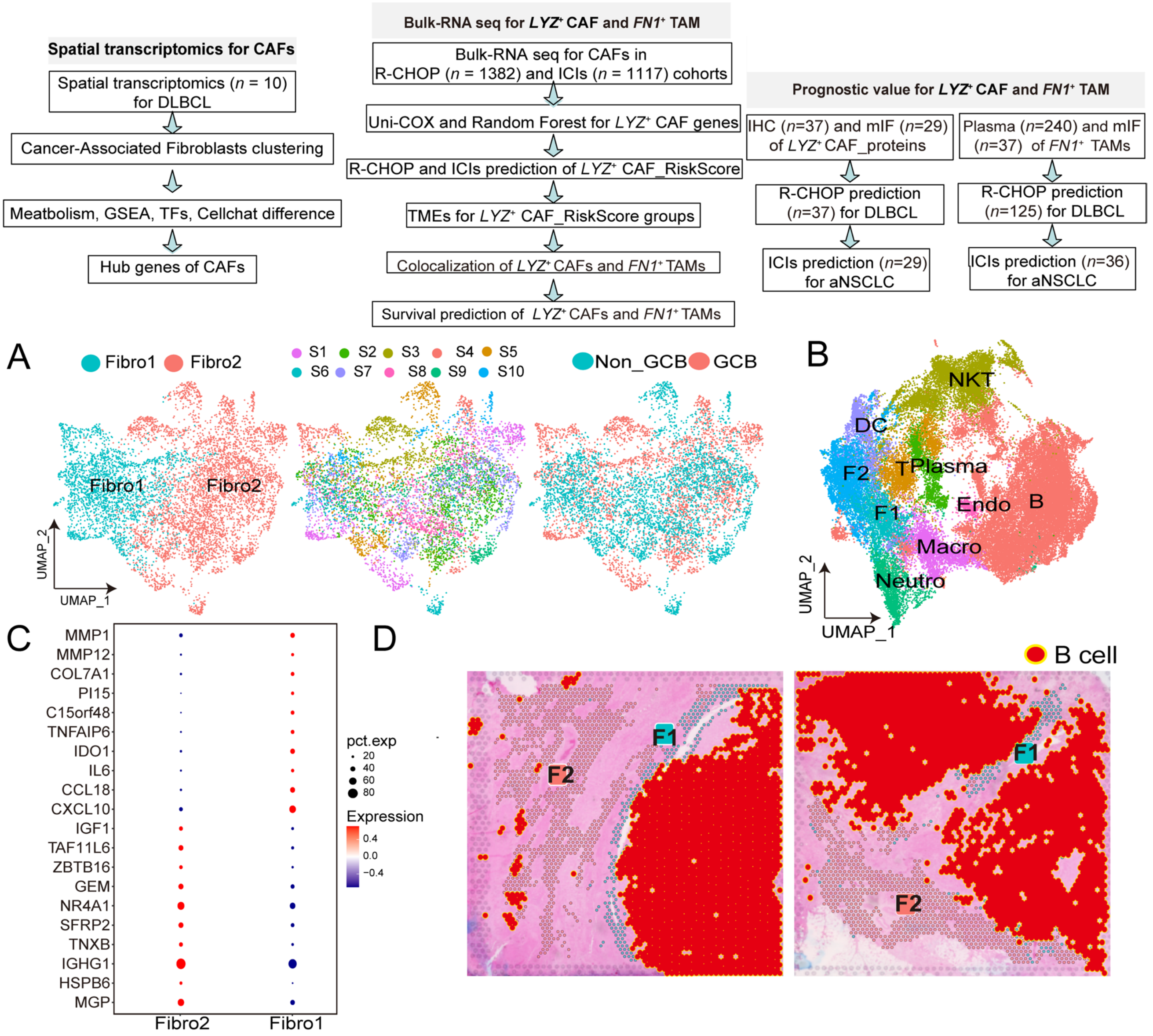

Fig. 1 Flowchart overview of the study and identification of cancer-associated fibroblast subgroups. **A** UMAP plot showing fibroblast cell types and their distribution across different origin cell groups. **B** UMAP plot displaying all cell types. **C** Dot plot illustrating the expression levels of fibroblast markers across CAF subclusters. **D** Representative spatial plots (S2 and S7) of fibroblast cell type annotations and HE staining. DLBCL: diffuse large B cell lymphoma; R-CHOP: rituximab, cyclophosphamide, doxorubicin: vincristine, and prednisone; ICIs: immune checkpoint inhibitors; CAF: cancer-associated fibroblast; GCB: germinal-center B cell-like; UMAP: uniform manifold approximation and projection; HE: hematoxylin and eosin

cell–cell communication, examining categories such as 'Secreted Signaling', 'ECM-Receptor', and 'Cell–Cell Contact' with a minimum cell count criterion of 3.

For a lymph node ST sample, CARD deconvolution and cell type annotation were performed. The 'CARD' package was used to deconvolute ST data based on four DLBCL scRNA-seq datasets from GSE182434. A 'CARD' object was created using the 'CreateCARDObject' function, and deconvolution was carried out with the 'CARD_deconvolution' function using default parameters. After preprocessing steps including SCTransform, PCA, and data integration via Harmony, ST spots were clustered into discrete groups using the 'FindClusters' function with a resolution parameter of

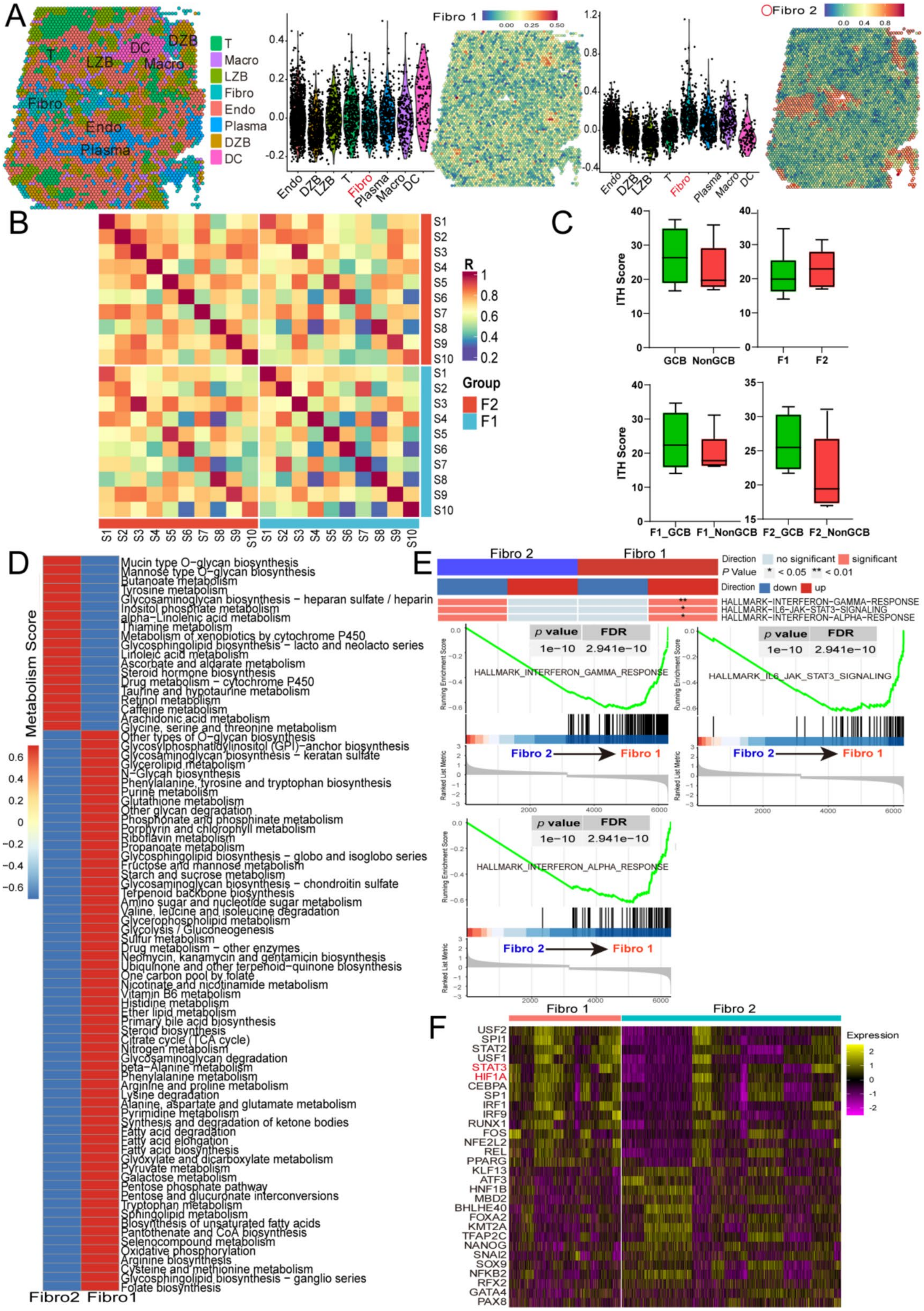

0.5. UMAP visualization of the first 30 principal components, performed with ‘RunUMAP’, provided a two-dimensional representation of the clusters. Marker genes were identified using ‘FindAllMarkers’ following ‘PrepSCTFindMarkers’, with genes considered if detected in at least 25% of cells within the cluster, exhibiting a Wilcoxon test *p* value < 0.05, and demonstrating a differential expression threshold of 0.25 log fold change

◂**Fig. 2** Metabolism and signaling enrichment atlas of different fibroblast subtypes and fibroblast2 enrichment in a lymph node sample. **A** Spatial plots showing cell type annotations and fibroblast2 enrichment in a lymph node sample. **B** Correlation of transcriptional profiles between fibroblast1 and fibroblast2 across ten samples. **C** ITH scores comparisons between GCB and non-GCB samples, fibroblast1 and fibroblast2, and GCB versus non-GCB samples within fibroblast1 and fibroblast2. **D** Heatmap of metabolism enrichment across different fibroblast cell types. **E** Hallmark pathways associated with different fibroblast cell types as determined by GSEA. **F** Heatmap representation of the top 20 highly variable transcription factor activities in fibroblast1 and fibroblast2. DZB: dark zone B cells; LZB: light zone B cells; ITH: intratumoral heterogeneity; and GCB: Germinal Center B cell

(logFC). These marker genes were cross-referenced with known cell types using the CellMarker (http://biocc.hrbmu.edu.cn/CellMarker/) and PanglaoDB (https://panglaodb.se/) databases. The ‘AddModuleScore’ function from the ‘Seurat’ package was used to calculate the fibroblast1 risk score.

Bulk-RNA sequencing analysis of cancer-associated fibroblasts and macrophages

Datasets GSE31212 (platform GPL570, $n = 470$), GSE181063 (platform GPL14951-11332, $n = 802$), and GSE136971 (platform GPL570, $n = 109$) were annotated for comprehensive analysis. Raw data were subjected to rigorous quality control using the ‘Affy’ package in R, which involved computing average values for multiple probes corresponding to a single gene. Univariate Cox analyses for overall survival (OS) were conducted using the ‘survival’ package. Results were visualized with scatter plots, risk score heatmaps, and time-dependent receiver operating characteristic (ROC) curves generated using the ‘ggrisk’ and ‘survminer’ packages, respectively. Optimal cutoff values for distinguishing high- and low-expression groups were determined with the ‘maxstat’ package in R. Tumor immune cell infiltration in all DLBCL patients was calculated using the IOBR package. Single-sample Gene Set Enrichment Analysis (ssGSEA) scores across cell types in GEO datasets were computed using the ‘GSVA’ package, leveraging marker genes specific to each cell type. For comparative analysis of mRNA expression of prognostic markers predicting R-CHOP and immunotherapy response, the Biomarker Exploration of Solid Tumors (BEST) (https://rookieutopia.hiplot.com.cn/app_direct/BEST/) and KM Plot databases (https://kmplot.com/analysis/) were used. Protein–protein interaction networks among markers were analyzed using the STRING website (https://cn.string-db.org/), and functional enrichment of markers was performed using the Metascape website (https://metascape.org/gp/index.html).

Plasma proteomics validation of DLBCL and aNSCLC samples

To investigate the fibroblast cells and macrophages marker’s autoantibodies (AAbs) in plasma, we performed HuProt high-density antigen microarray (~ 21,000 proteins) in 20 DLBCL and 36 aNSCLC patients and antibody microarray targeting 551 unique human proteins in 125 DLBCL patients and 79 healthy controls [20–22].

The detailed experimental procedures were described previously [20–22]. For HuProt high-density antigen microarray, proteins with GST tags were synthesized using a yeast expression system and printed onto 24 blocks on glass substrates. Microarrays were removed from −80 °C and blocked with 5% BSA in PBS-T for 1.5 h at room temperature. Then, microarrays were incubated with plasma samples (diluted 1:1000 in 5% BSA) for 1 h at room temperature. After three washes with 0.1% PBS-T, Alexa Fluor 647 goat anti-human IgG (diluted in 5% BSA) was added and incubated for 1 h in darkness, followed by three more washes with 0.1% PBS-T. Last, microarrays were air-dried and scanned with a GenePix 4300A using a 635 nm laser, and signal intensities of IgG for each protein were analyzed with GenePix Pro v.6.0 software. For antibody microarray targeting 551 unique human proteins, antibody microarrays on glass were blocked with 500 µl of 5% milk (w/v) per well for 1 h, followed by incubation with biotinylated plasma proteins at 4 °C overnight (8 h). After washing three times with PBS containing 5% Tween-20, arrays were incubated with 2 µg/ml streptavidin-Cy3 for 1 h at room temperature and then washed again. Fluorescence was detected at 532 nm using a GenePix 4300A scanner, and signal intensity was extracted with GenePixPro7 software (Molecular Devices). The median pixel intensity of each spot was adjusted by subtracting the background intensity to correct for nonspecific binding or spatial heterogeneity. Average intensities across duplicate spots were calculated, and spots with intensities below the background were marked as missing values.

Immunohistochemistry validation

All patient samples underwent hematoxylin–eosin staining and were meticulously reviewed by two experienced pathologists to identify cancer lesions. IHC was performed on FFPE samples following dewaxing and heat-induced antigen retrieval. The samples were washed and treated with a 3% hydrogen peroxide solution to quench endogenous peroxidase activity. Primary antibodies were then applied to FFPE samples, including rabbit anti-human IgG antibodies specific to lysozyme (LYZ, ab108508, Abcam) and leukocyte immunoglobulin-like receptor B4 (LILRB4, #55107, Signalway Antibody), at dilutions of 1:2000 and 1:2000, respectively, after blocking with rabbit serum. Following

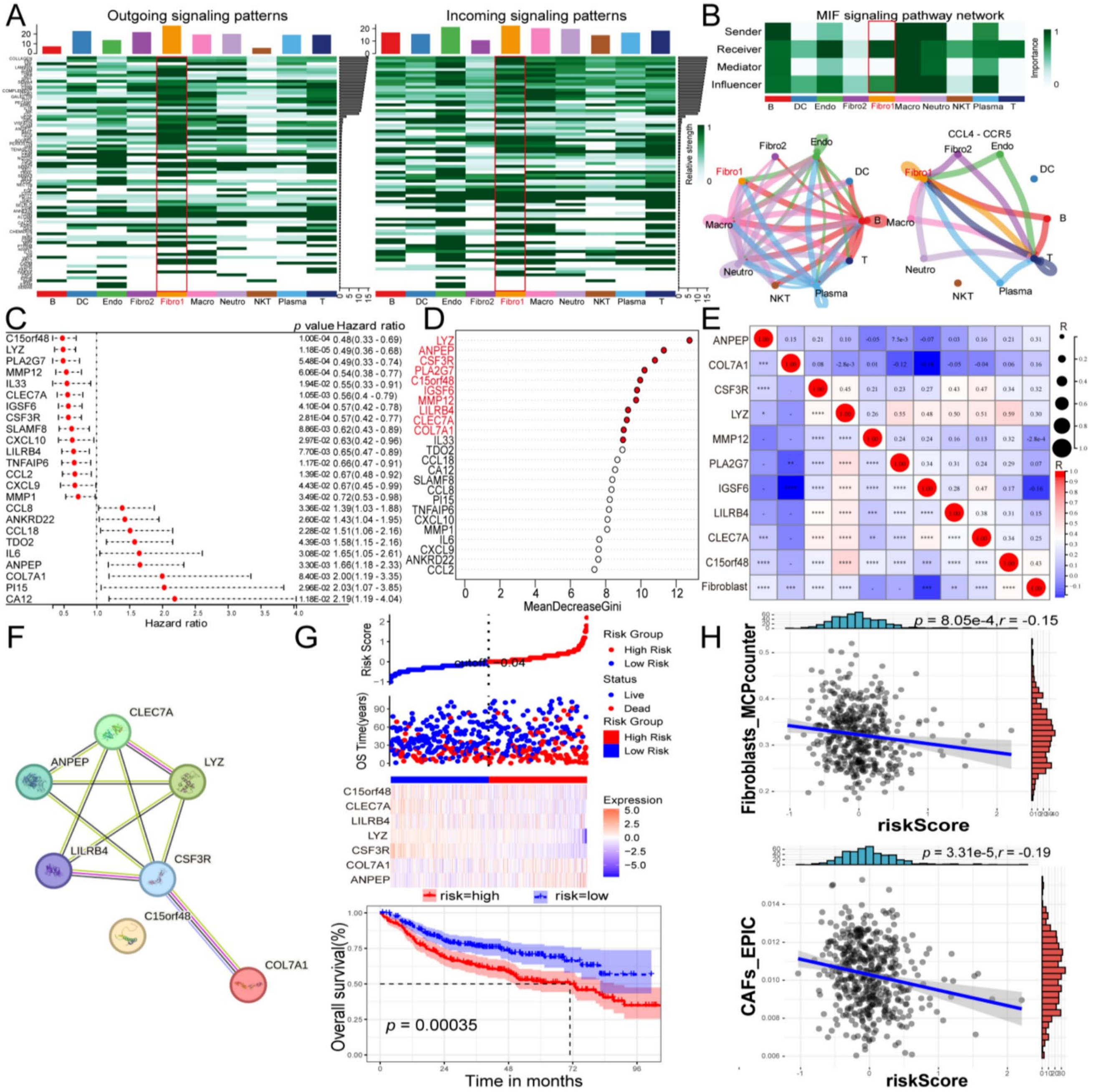

Fig. 3 Cell–cell communications across all cell types and identification of fibroblast1 maker genes and performance of seven maker gene-based risk scores in predicting survival of DLBCL receiving R-CHOP in GSE31212. **A** Heatmap of cell–cell communication network, showing incoming and outgoing signaling analysis. **B**, **C** Heatmap, and circular plot illustrating the relative importance of cell groups in the MIF and CCL4-CCR5 signaling networks, based on four network centrality measures. **C** Univariate Cox analysis of 24 fibroblast1 maker genes for OS. **D** Random forest analysis of 24 fibroblast1 maker genes for OS. **E** Correlation of 10 fibroblast2 maker genes with the fibroblast score. **F** Protein–protein interaction networks of 7 fibroblast1-related proteins. **G** Scatter plots and heatmaps for the seven fibroblast1-based risk scores, with Kaplan–Meier curves for OS. **H** Correlation of the 7 fibroblast1 gene-based risk score with fibroblast score calculated by MCP counter and EPIC. MIF: macrophage migration inhibitory factor; DLBCL: diffuse large B cell lymphoma; R-CHOP: rituximab, cyclophosphamide, doxorubicin: vincristine, and prednisone; and OS: overall survival

incubation, the samples were treated with a 1:200 dilution of HRP-labeled goat anti-rabbit IgG secondary antibody (GB23303, Servicebio) for 50 min at room temperature. Diaminobenzidine was used for color development, and the nuclei were counterstained with hematoxylin (G1004, Servicebio). Results were examined under a white light microscope (E100, Nikon) and quantified using CaseViewer 2.4 (3DHISTECH, Hungary) software.

Protein expression were quantified by *H* Score. The *H* Score was calculated based on the intensity of the stain and the percentage of positive tumor cells, with scores ranging from 0 to 300. Stain intensity was classified as negative (0 scores), weak (1 score), moderate (2 scores), and strong (3 scores) stain, and the percentage of positive cells was scored from 0 to 100. *H* Score was calculated as the product of intensity and percentage. *H* Scores below 60 were determined as low expression, while *H* Scores greater than or equal to 60 were considered high expression.

Multiple immunofluorescence

FFPE tissue sections, 4–5 μm in thickness, were prepared and subjected to dewaxing and rehydration. Antigen retrieval was performed, followed by blocking of endogenous peroxidase activity using an antibody blocking solution. Sequential immunostaining was conducted for each target antigen. Primary antibodies included rabbit anti-human IgG antibody LYZ (ab108508, dilution 1:2000, Abcam), LILRB4 (#55107, dilution 1:2000, Signalway Antibody), COL3A1 (#63034S, dilution 1:3000, Cell Signaling Technology), FN1 (#26836S, dilution 1:2000, Cell Signaling Technology), CD68 (ab303565, dilution 1:1000, Abcam), and mouse anti-human pan-cytokeratin IgG antibody (GB122053, dilution 1:2000, Servicebio) and COL1A2 (sc-393573, dilution 1:2000, Santa Cruz Biotechnology). These were followed by incubation with secondary antibodies: HRP-labeled goat anti-rabbit IgG (GB23303, dilution 1:500, Servicebio) for LYZ, LILRB4, COL3A1, FN1, and CD68, and HRP-labeled goat anti-mouse IgG (GB23301, dilution 1:500, Servicebio) for pan-cytokeratin and COL1A2. Tyramide signal amplification (TSA) was used, with subsequent microwave treatment to remove the TSA-antibody complex, allowing for additional rounds of antibody labeling. iF555-Tyramide (G1233, dilution 1:500, Servicebio) was used for LILRB4, iF488-Tyramide (G1231, dilution 1:500, Servicebio) for LYZ, and iF647-Tyramide (G1232, dilution 1:500, Servicebio) for pan-cytokeratin. iF488-Tyramide (G1233, dilution 1:500, Servicebio) was used for COL1A2, iF440-Tyramide (G1231, dilution 1:500, Servicebio) for COL3A1, iF594-Tyramide (G1232, dilution 1:500, Servicebio) for FN1, and iF647-Tyramide (G1232, dilution 1:500, Servicebio) for CD68. After immunostaining, cell nuclei were counterstained with 4',6-diamidino-2-phenylindole (DAPI), and slides were coverslipped for scanning. Microscopy (ECLIPSE C1, Nikon) and scanning (Pannoramic MIDI, 3DHISTECH) were used for result interpretation. Quantification of the number and percentage of positive cells was performed using CaseViewer 2.4 (3DHISTECH) and ImageJ software. Two experienced pathologists independently reviewed all results. During the validation of macrophage-associated genes in the DLBCL mIF cohort, the staining for the APOE antibody failed despite multiple optimization attempts. As a result, APOE could not be included in the validation analysis. The remaining three proteins (FN1, COL1A2, and COL3A1) were successfully validated using mIF, and their prognostic significance was confirmed in DLBCL. This limitation is acknowledged, and future studies will explore alternative approaches to validate APOE expression and its role in the tumor microenvironment.

Statistical analysis

All statistical analyses were conducted using R version 4.3.1, Sanger plot (http://www.sangerbox.com), and Hiplot (https://hiplot.com.cn/home/index.html). The 'maxstat' package in R was used to determine the optimal cutoff value for categorizing high- and low-expression groups in survival analysis. A significance level of $p < 0.05$ (two-tailed) was considered statistically significant for all analyses.

Results

Study design

The overall study design, as illustrated in Fig. 1, comprised three phases: (1) spatial transcriptomics for fibroblast subtypes in DLBCL samples ($n = 10$) and a lymph node sample ($n = 1$); (2) bulk-RNA sequencing to assess the prognostic value of *LYZ*$^+$ fibroblasts and their colocalization with *FN1*$^+$ macrophages in DLBCL samples ($n = 1382$) treated with R-CHOP and aNSCLC samples ($n = 1117$) treated with ICIs; and (3) IHC and mIF validation for the prognostic value of *LYZ*$^+$ fibroblasts markers in DLBCL samples ($n = 37$) receiving R-CHOP and aNSCLC samples ($n = 29$) receiving ICIs and AAbs validation for the prognostic value of *FN1*$^+$ macrophages markers in DLBCL samples ($n = 125$) receiving R-CHOP and aNSCLC samples ($n = 36$) receiving ICIs. Detailed clinical characteristics are provided in Tables S1 and S2.

Fibroblast typing by ST: metabolism, GSEA, TFs and cell–cell communication of fibroblasts

For the 10 ST samples, we performed sample harmony integration, CARD deconvolution and cell type annotation, and intratumoral heterogeneity score analysis in accordance with our original study [16]. Following harmony integration, fibroblast cells were clustered into distinct types, with clear separation between patient sample distributions and

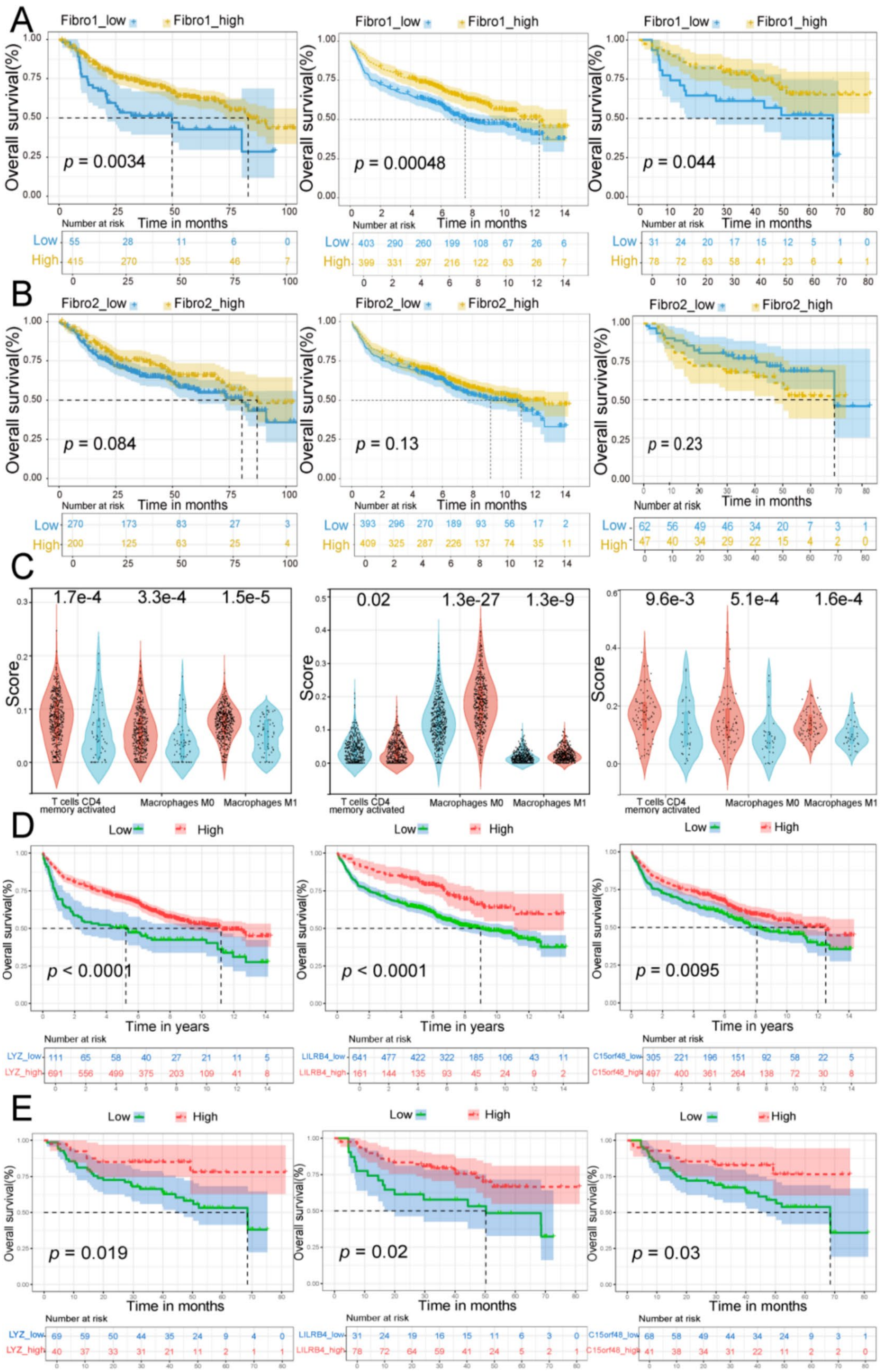
A
Fibro1_low
Fibro1_high
Overall survival(%)
p = 0.0034
p = 0.00048
p = 0.044
Time in months
Number at risk
Low
High
B
Fibro2_low
Fibro2_high
p = 0.084
p = 0.13
p = 0.23
C
Score
1.7e-4
3.3e-4
1.5e-5
0.02
1.3e-27
1.3e-9
9.6e-3
5.1e-4
1.6e-4
T cells CD4 memory activated
Macrophages M0
Macrophages M1
D
Low
High
p < 0.0001
p < 0.0001
p = 0.0095
Time in years
LYZ_low
LYZ_high
LILRB4_low
LILRB4_high
C15orf48_low
C15orf48_high
E
p = 0.019
p = 0.02
p = 0.03
Time in months

◂**Fig. 4** Performance of fibroblast1 and fibroblast2 in predicting survival in DLBCL receiving R-CHOP in GSE31212, GSE181063, and GSE136971. **A**, **B** Kaplan–Meier analysis of OS based on fibroblast1 and fibroblast2 (calculated by ssGSEA). **C** Distribution of CD4$^+$ T cell, macrophages M0, and M1 cell types in high and low fibroblast1 risk groups. **D**, **E** Performance of fibroblast1_markers (*LYZ*, *LYLRB4*, and *C15orf48*) in predicting OS in DLBCL. DLBCL: diffuse large B cell lymphoma; R-CHOP: rituximab, cyclophosphamide, doxorubicin: vincristine, and prednisone; and OS: overall survival

germinal-center B cell-like (GCB) and non-GCB groups (Fig. 1A). PCA clustering identified two distinct fibroblast subtypes (Fig. 1B), as illustrated in the dot plot (Fig. 1C). Fibroblast subtype 1 (F1, 4640 spots) exhibited higher expression of *MMP1, MMP12, COL7A1, PI15, c15orf48, TNFAIP6, IDO1, IL6, CCL18*, and *CXCL10*, and fibroblast subtype 2 (F2, 2374 spots) showed elevated expression of *MGP, HSPB6, IGHG1, TNXB, SFRP2, NR4A1, GEM, ZBTB16, TAF11L6*, and *IGF1* (Fig. 1C, Table S3). F1 and F2 exhibited distinct regional distribution patterns in HE staining (Fig. S1 A-B), with F1 located near the tumor region and F2 positioned farther from it, as demonstrated in the representative staining plots (Fig. 1D). The distribution of cell types across samples is detailed in Table S4 and Fig. S1C.

To investigate the distribution of two types of tumor-associated fibroblasts in normal lymph node tissue, ST samples from a normal lymph node, obtained from the SpatialTME database (http://labwebsite.yelab.site:1234/#!/), were analyzed. Quality control of the lymph node sample revealed 4039 detected spots. The nCounts, percentage of mitochondrial genes, and nFeatures for this sample are shown in Fig. S2A. PCA clustering, along with reference to single-cell annotation databases (CellMarker and PangLaoDB), identified eight distinct cell types (Fig. S2B). Reference markers are detailed in the heatmap (Fig. S2C) and Table S5. Consistency between CARD deconvolution results and manual annotation is illustrated in Fig. S3A-B. Gene markers ($FC > 1.0$, $p < 0.05$) used for calculating F1 and F2 in the lymph node sample revealed that F1 exhibited the highest infiltration of dendritic cells, while F2 was most abundant in normal fibroblast cells (Fig. 2A).

Transcriptional profiles correlation analysis between F1 and F2 cells across ten samples revealed that F1 cells exhibited a higher correlation than F2 cells (Fig. 2B, Table S6). This finding was consistent with the intratumoral heterogeneity scores (Fig. 2C, Table S7), and GCB patients showed a higher correlation than non-GCB patients (Fig. 2C). F1 cells demonstrated elevated metabolic activity in most (60/79) metabolic pathways (Fig. 2D) and exhibited significant enrichment in interferon gamma response, IL6-JAK-STAT3 signaling, and interferon alpha response ($p < 0.05$) (Fig. 2E). Enhanced TF activities were observed in F1 cells for USF2, SPI1, STAT2, USF1, STAT3, HIF1A, CEBPA, SP1, IRF1, IRF9, RUNX1, FOS, NFE2L2, REL, and PPARG (Fig. 2F). Among 54 detected pathways across 10 cell types, the macrophage migration inhibitory factor (MIF) pathway emerged as a prominent signaling mode, both incoming and outgoing (Fig. 3A). Specifically, macrophages and malignant B cells were identified as the primary senders, with F1 cells displaying greater receptivity to the MIF pathway compared to F2 cells (Fig. 3B).

LYZ$^+$ fibroblasts risk score in bulk sequencing

To assess the prognostic value of F1 and F2 cells, 33 genes associated with F1 ($FC > 1.2$, $p < 0.05$) and 15 genes associated with F2 ($FC > 1.0$, $p < 0.05$) were selected. Univariate Cox analyses revealed that 24 genes associated with F1 had prognostic value for OS ($p < 0.05$) (Fig. 3C). The top 10 genes (*LYZ, ANPEP, CSF3R, PLA2G7, C15orf48, IGSF6, MMP12, LILRB4, CLEC7A*, and *COL7A1*) were identified using random forest analysis (Fig. 3D). Correlation analysis of gene markers with fibroblast score (calculated by MCP counter) indicated that seven genes (*LYZ, ANPEP, CSF3R, C15orf48, LILRB4, CLEC7A*, and *COL7A1*) were positively correlated ($R > 0$, $p < 0.05$) with the fibroblast score (Fig. 3E). Protein–protein interaction network analysis demonstrated interactions among these F1 signature genes (Fig. 3F). So F1 was named as *LYZ*$^+$ fibroblasts. A risk score model based on these seven *LYZ*$^+$ fibroblasts markers was constructed using the formula: risk score = Σ (Expression * Coefficient), with coefficients determined by Cox regression in the 'rms' package. Samples were stratified into high- and low-risk groups based on the optimal cutoff value (Fig. 3G). The high-risk score group exhibited significantly worse OS ($p < 0.05$) (Fig. 3G) compared to the low-risk score group. The *LYZ*$^+$ fibroblasts risk score showed a negative correlation ($R < 0$, $p < 0.05$) with fibroblasts (as calculated by MCP counter) and cancer-associated fibroblasts (CAFs, as calculated by EPIC) in GSE31212 (Fig. 3H), with similar results observed in GSE181063 and GSE136971 (Fig. S4A-B).

Seven genes for *LYZ*$^+$ fibroblasts and 15 genes for F2 were evaluated using ssGSEA. *LYZ*$^+$ fibroblasts demonstrated a significant prognostic value for OS ($p < 0.05$) across three GEO datasets (Fig. 4A), whereas F2 did not ($p > 0.05$) (Fig. 4B). According to CIBERSORT analysis, the high-risk score group exhibited a more robust immune environment, characterized by elevated ($p < 0.05$) infiltration of activated CD4$^+$ T cells, M0 macrophages, and M1 macrophages (Fig. 4C). Among the seven *LYZ*$^+$ fibroblasts markers (*LYZ, ANPEP, CSF3R, C15orf48, LILRB4, CLEC7A*, and *COL7A1*), *LYZ* and *LILRB4* showed significant prognostic value for OS across three GEO datasets ($p < 0.05$) (Fig. 4 D-E). *LYZ* also demonstrated prognostic significance in six DLBCL datasets ($n = 1095$, $p < 0.05$) (Fig. S5A) and was associated with higher IGHM and MUC16 gene mutations in patients with lower LYZ expression ($p < 0.05$) (Fig. S5B).

(*Abbreviation: DLBCL: diffuse large B-cell lymphoma; R-CHOP:* rituximab, cycolphosphamide, doxorubicin: vincristine, and prednisone*; OS: overall survival.*)

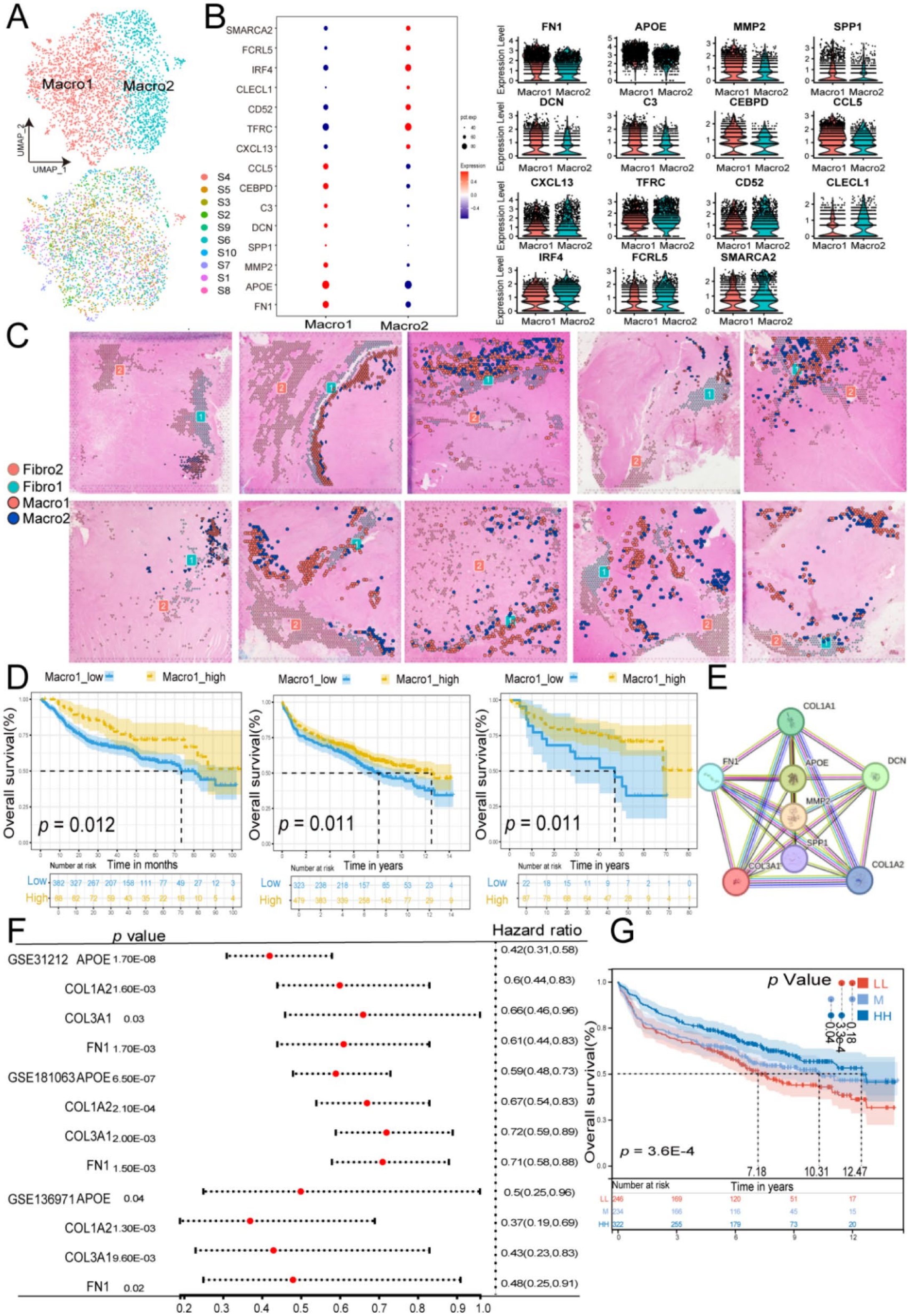

◂**Fig. 5** Identification of macrophage subgroups and their colocalization with fibroblast1 in predicting survival of DLBCL receiving R-CHOP in GSE31212, GSE181063, and GSE136971. **A** UMAP plot showing macrophage cell types and their distribution across different origin cell groups. **B** Dot plot and violin plot illustrating the expression levels of macrophage markers. **C** Colocalization of macrophage1 with fibroblast1 in ten samples. **D** Kaplan–Meier analysis for OS based on macrophage1 (calculated by ssGSEA). **E, F** Protein–protein interaction networks of 8 macrophage1-related proteins and univariate Cox analysis of 4 macrophage1 maker genes for OS. **G** OS stratified by the fibroblast1 marker-based risk score combined with macrophage1 in GSE181063, and distribution of fibroblasts, macrophages M0, and M1 cell types in high and low macrophage1 risk groups. DLBCL: diffuse large B cell lymphoma; R-CHOP: rituximab, cyclophosphamide, doxorubicin: vincristine, and prednisone; UMAP: uniform manifold approximation and projection; and OS: overall survival

Additionally, *LYZ* and *LILRB4* were found to be elevated in responders compared to non-responders among pan-cancer patients (melanoma, NSCLC, and breast cancer) receiving immunotherapy (including CAR-T and anti-PD-1/PD-L1/CTLA-4/MAGE-A3) ($p < 0.05$) (Fig. S5C) and were associated with superior progression-free survival (PFS) ($p < 0.05$) (Fig. S5D). Higher levels of *LYZ* and *LILRB4* were also linked to enrichment in the IL6-JAK-STAT3 signaling pathway ($p < 0.001$) (Fig. S5E). *LYZ* and *LILRB4* are highly expressed in dendritic cells and macrophage cells in single-cell samples of NSCLC ($n = 8$) (Fig. S6A). Patients with higher *LYZ* or *LILRB4* expressions also demonstrated longer OS in the GSE218989 ($n = 339$) compared to those with lower *LYZ* or *LILRB4* expression ($p < 0.05$) (Fig. S6B).

Macrophage typing by ST and their prognostic value in bulk-seq

Based on cell–cell communication results and differences in immune cell infiltration observed in bulk-RNA sequencing, macrophages were categorized into distinct types at the ST level. Macrophage cells were divided into two subtypes, with patient sample distributions showing a mix of GCB and non-GCB groups (Fig. 5A). As illustrated in the dot plot and UMAP plots (Fig. 5B, Fig. S7A), macrophages1 (M_1, 1786 spots) exhibited higher expression levels of *CCL5, CEBPD, C3, DCN, SPP1, MMP2, APOE*, and *FN1*, whereas macrophages2 (M_2, 1078 spots) showed elevated expression of *CXCL13, TFRC, CD52, CLECL1, IRF4, FCRL5*, and *SMARCA2* (Fig. 5B and Table S8). M_1 was named as *FN1*$^+$ macrophages. The distribution of cell types across samples is detailed in Fig. S7B and Table S9. Correlations between *FN1*$^+$ macrophages and M_2 cells across ten samples are shown in Fig. S7C and Table S10. *FN1*$^+$ macrophage cells demonstrated enriched activity in the HALLMARK pathways of epithelial mesenchymal transition, IL6-JAK-STAT3 signaling, complement, angiogenesis, and coagulation ($p < 0.05$) (Fig. S7D). Enhanced TF activities for SP3, PRDM14, SMAD3, JUN, RUNX1, SP1, and HNF4G were specifically observed in *FN1*$^+$ macrophage cells (Fig. S7E). Colocalization of *LYZ*$^+$ fibroblasts and *FN1*$^+$ macrophage cells was evident across ten samples in Fig. 5C. Patients with higher *FN1*$^+$ macrophage cell infiltration (top 10 genes calculated by ssGSEA) also showed superior OS across GEO datasets ($p < 0.05$) (Fig. 5D). Protein–protein network analysis revealed interactions among these *FN1*$^+$ macrophage signatures (Fig. 5E). Four genes (*APOE, COL1A2, COL3A1,* and *FN1*) demonstrated prognostic value for OS across three GEO datasets ($p < 0.05$) (Fig. 5E). Patients with higher *FN1*$^+$ macrophage and *LYZ*$^+$ fibroblasts cell counts exhibited the best OS compared to other groups ($p < 0.05$) (Fig. 5F).

Validation of prognostic value for *LYZ*$^+$ fibroblasts and *FN1*$^+$ macrophages markers in DLBCL and aNSCLC patients receiving immunotherapy

To validate the generalizability of our findings beyond DLBCL, we extended our analysis to NSCLC samples. NSCLC was selected as a representative solid tumor model due to its well-characterized TME and the availability of large-scale clinical and transcriptomic data. This comparative approach allowed us to explore whether the fibroblast-immune cell interactions identified in DLBCL are conserved in other cancer types, providing broader insights into their potential as therapeutic targets. To validate the prognostic value of *FN1*$^+$ macrophages markers, we conducted IHC analysis of LYZ and LILRB4, and mIF analysis of FN1, COL1A2, COL3A1, and CD68 in 37 DLBCL patients treated with R-CHOP, along with mIF analysis of LYZ and LILRB4 in 29 aNSCLC patients receiving ICIs (Tables S1 and S2). In DLBCL patients, Fig. S8 presents the scoring criteria for LYZ and LILRB4, categorized as strong, moderate, weak, and negative expression. Representative IHC staining of LYZ is illustrated for a patient with prolonged PFS (1697 days) and another with short PFS (341 days), alongside LILRB4 staining in a patient with long PFS (826 days) and one with short PFS (64 days), and according to HE images, they were highly expressed in fibroblasts (Fig. 6A). PFS analysis demonstrated the prognostic significance of LYZ protein expression in this cohort ($p < 0.05$) (Fig. 6B), while not LILRB4 protein expression. In aNSCLC patients treated with ICIs, representative mIF staining for DAPI, LYZ, LILRB4, and pan-cytokeratin is shown in Fig. 6C, with LYZ and LILRB4 intensity identified as significant predictor of OS ($p < 0.05$) (Fig. 6D). COL3A1 and *FN1*$^+$ macrophages intensity identified as significant predictor of PFS ($p < 0.05$) (Fig. 6E).

To further validate the prognostic value of *FN1*$^+$ macrophages markers, we performed an AAb assay using the HuProt high-density platform on samples from 20 DLBCL and 36 NSCLC patients, as well as utilizing 551

Fig. 6 Prognostic value of LYZ and LILRB4 proteins in DLBCL receiving R-CHOP ($n = 37$, 10X) and aNSCLC receiving ICIs ($n = 29$, 2X and 10X). **A** Representative IHCs staining of LYZ in patient 1 (PFS = 1697 days) and patient 2 (PFS = 341 days), LILRB4 in patient 3 (PFS = 64 days) and patient 4 (PFS = 826 days). **B** Kaplan–Meier survival curves of PFS grouped by the LYZ and LILRB4 expression in DLBCL. **C** Representative mIF staining of LYZ, LILRB4, and pan Cytokeratin. **D** Kaplan–Meier survival curves of OS grouped by the LYZ and LILRB4 expression in aNSCLC. **E** Kaplan–Meier survival curves of PFS grouped by the COL3A1 expression and *FN1*$^+$ macrophages in DLBCL. DLBCL: diffuse large B cell lymphoma; R-CHOP: rituximab, cyclophosphamide, doxorubicin: vincristine, and prednisone; aNSCLC: advanced non-small cell lung cancer; ICIs: immune checkpoint inhibitors; IHC: immunohistochemistry; PFS: progression-free survival; mIF: multiple immunofluorescence; and OS: overall survival

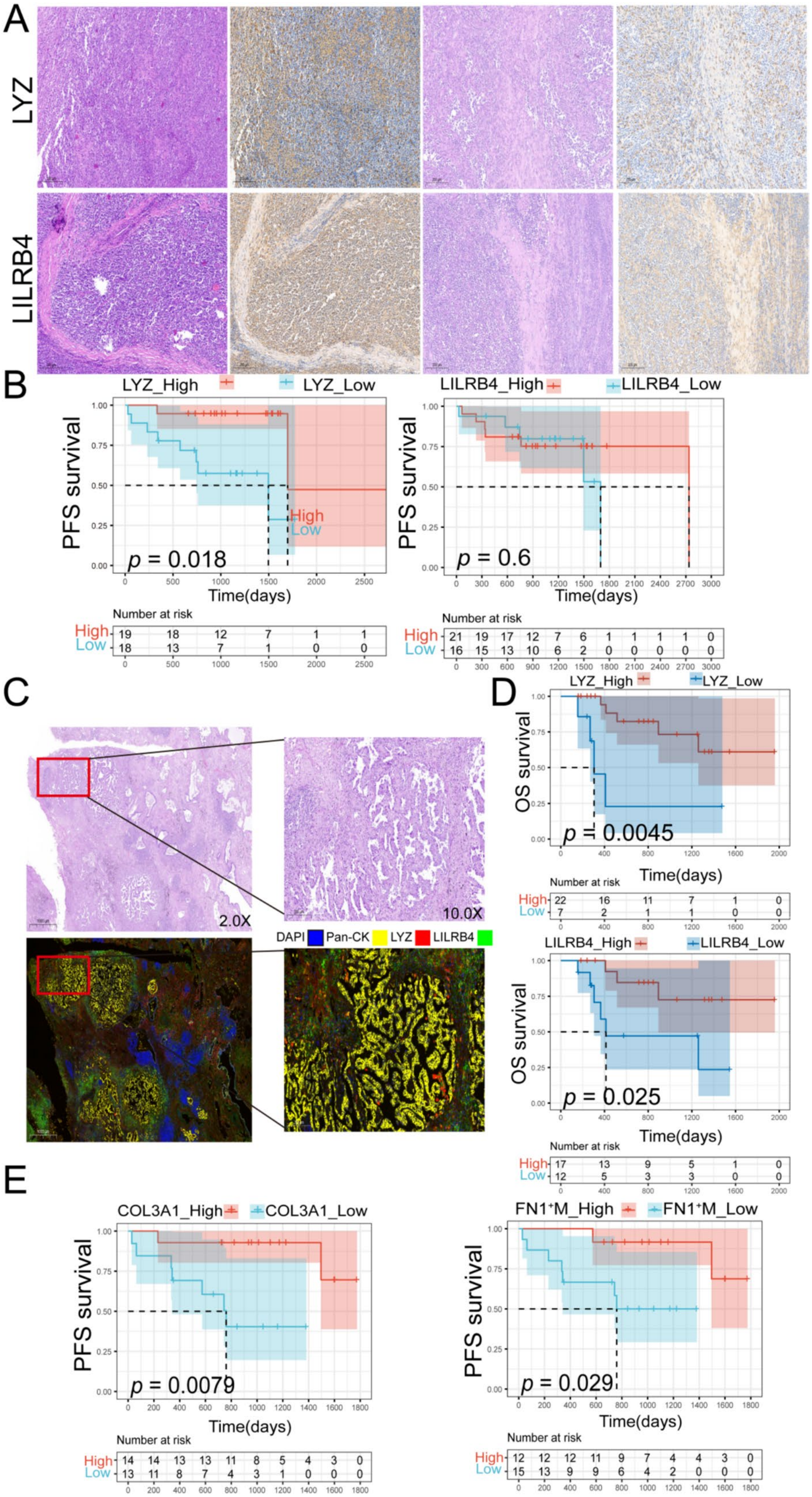

unique human protein microarrays on 125 DLBCL samples (Tables S1 and S2). For the 20 DLBCL samples, we employed fold change > 1.0 and $p < 0.05$ as cutoffs for selecting candidate AAbs (Fig. 7A, Table S11). Among these, the COL1A2 AAb was elevated ($p = 0.06$) in the complete remission group compared to none-complete remission group. Representative density staining of the COL1A2 AAb from a patient with long PFS (2011 days) and another with short PFS (193 days) is shown in Fig. 7A. Patients with higher COL1A2 AAb levels demonstrated superior PFS ($p < 0.05$) (Fig. 7B). Additionally, elevated COL1A2 and COL3A1 mRNA expression was associated with improved OS in the GSE218989 ($p < 0.05$) (Fig. 7C). In the 36 NSCLC samples, high levels of COL1A2 and COL3A1 AAbs were also correlated with better PFS ($p < 0.05$) (Fig. 7C). Furthermore, in 125 DLBCL samples compared to 79 healthy controls, FN1 AAb levels were significantly higher in DLBCL ($p < 0.05$), and elevated FN1 AAb levels were associated with improved PFS ($p < 0.05$) (Fig. 7D).

Discussion

Several studies have focused on CAFs and DLBCL prognosis [23–26]. B. Apollonio, et.al found that DLBCL exposure reprograms key immunoregulatory pathways in fibroblasts, including the transition from homeostatic chemokine to inflammatory chemokine expression, as well as an increase in antigen-presenting molecules. Activated fibroblasts inhibit the activity of $CD8^+$ tumor-infiltrating lymphocytes through the abnormal expression of PD-1 ligands (PD-L1 and PD-L2) [23]. Five genes (*A2M, FN1, CTSB, MMP9,* and *SPARC*) were reported to have association with CAFs infiltration in DLBCL [24]. The gene signature of DLBCL stroma was correlated with better survival in B cell lymphoma, possibly due to CAFs attracting and trapping malignant B cells, thereby preventing their dissemination to new anatomical sites [25], like adipose tissue-derived fibroblasts can suppress the formation of plasmablasts and induce the formation of regulatory B cells [26]. However, whole tissues provide average gene expression levels, which fail to reveal the differences in cellular heterogeneity within tumors. Additionally, single-cell transcriptomics studies focused on DLBCL, such as GSE182434 [12], did not include fibroblast cells. In contrast, spatial transcriptomics effectively addresses these issues. While our previous work [16] highlighted the role of TAMs and high glycolysis B cells in shaping an exhausted immune microenvironment, the current study reveals the critical role of fibroblast-macrophage interactions, particularly LYZ^+ fibroblasts and $FN1^+$ macrophages, in determining DLBCL prognosis. These findings expand our understanding of the DLBCL TME and identify novel therapeutic targets with potential relevance across cancer types.

This study employed a multi-phase design to investigate the interactions between fibroblast and macrophage subtypes in DLBCL. The research commenced with spatial transcriptomics to categorize fibroblast subtypes, followed by bulk-RNA sequencing to evaluate the prognostic implications of LYZ^+ fibroblasts and $FN1^+$ macrophages in DLBCL. Subsequent validation through IHC and mIF revealed a significant association between high LYZ^+ fibroblast scores and improved patient prognosis, alongside increased infiltration and colocalization of $FN1^+$ macrophages. Notably, key prognostic markers, including LYZ, LILRB4, COL1A2, COL3A1, and FN1, were identified as critical indicators for survival in DLBCL and NSCLC patients.

Lysozyme (*LYZ*), which encodes lysozyme, is a component of the innate immune system produced by various cells, exhibiting antibacterial properties and showing high expression in mucus and saliva, with some immunosuppressive effects [27–29]. LYZ can promote fibroblast proliferation through the JAK/STAT3 signaling pathway [30]. Yu-Jie Zhou et al. discovered a LYZ^+ epithelial cells associated with traditional serrated adenoma in colorectal cancer [31]. In DLBCL, studies have found that higher levels of *LYZ* were associated with longer OS [32–34], and *LYZ* was positively correlated with macrophage infiltration in Hodgkin lymphoma [35]. Additionally, *LYZ* could inhibit the growth of human gastric cancer and lung cancer fibroblasts [36]. Consistent with our findings that LYZ is associated with favorable prognosis in DLBCL. LYZ^+ fibroblasts were associated with higher macrophage infiltration, high transcription factor activity of HIF1A [37] and STAT3 [38], usually activated in CAF and promotes CAF activation. In NSCLC, previous studies have indicated that fibroblasts were linked to poorer prognosis. We predict that LYZ, highly expressed in dendritic cells and macrophages in NSCLC, may exert its effects by inhibiting fibroblast proliferation.

Fibroblast proliferation was increased in co-culture with exosomes secreted by macrophages, and the expression levels of Collagen type I alpha 2 (*COL1A2*), Collagen type III alpha 1 (*COL3A1*), and Fibronectin 1 (*FN1*) were significantly elevated [44]. *FN1* is a key member of the extracellular matrix glycoprotein family and has been found to be widely expressed in various cell types. It mediates the interaction between cells and the extracellular matrix, playing a role in cell adhesion, migration, differentiation, growth of immune cells [39], and can regulate macrophage adhesion, playing an important role in the inflammatory response [40]. FN1 has garnered increasing attention due to its relationship with tumor progression and its potential value as a therapeutic target in cancer immunotherapy [41–43]. In various tumors, including liver cancer [44], pancreatic ductal

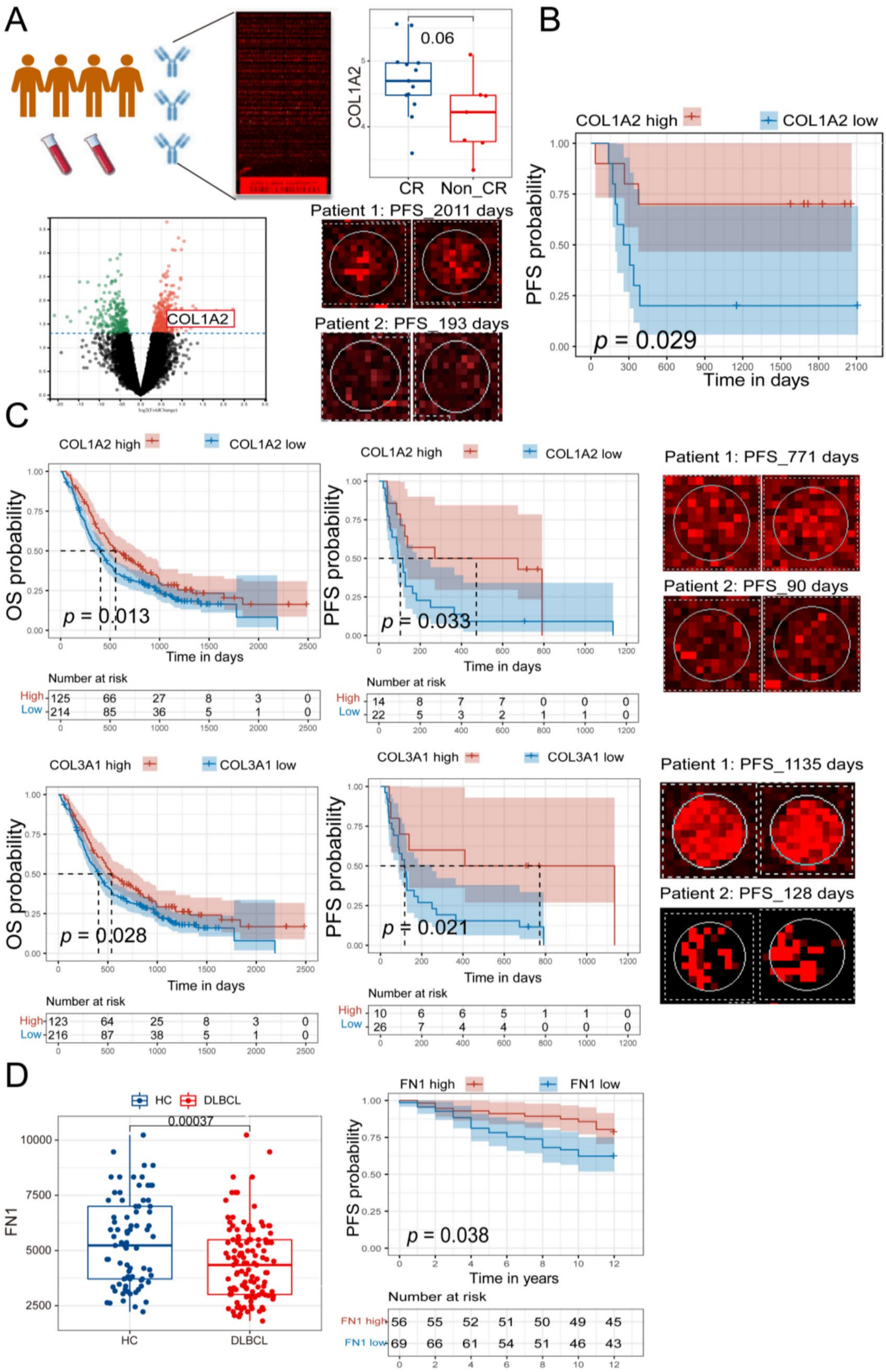
A
0.06
COL1A2
CR
Non_CR
COL1A2
Patient 1: PFS_2011 days
Patient 2: PFS_193 days
B
COL1A2 high
COL1A2 low
PFS probability
p = 0.029
Time in days
C
COL1A2 high
COL1A2 low
OS probability
p = 0.013
Time in days
Number at risk
High 125 66 27 8 3 0
Low 214 85 36 5 1 0
PFS probability
p = 0.033
Time in days
Number at risk
High 14 8 7 7 0 0 0
Low 22 5 3 2 1 1 0
Patient 1: PFS_771 days
Patient 2: PFS_90 days
COL3A1 high
COL3A1 low
OS probability
p = 0.028
Time in days
Number at risk
High 123 64 25 8 3 0
Low 216 87 38 5 1 0
PFS probability
p = 0.021
Time in days
Number at risk
High 10 6 6 5 1 1 0
Low 26 7 4 4 0 0 0
Patient 1: PFS_1135 days
Patient 2: PFS_128 days
D
HC
DLBCL
0.00037
FN1
FN1 high
FN1 low
PFS probability
p = 0.038
Time in years
Number at risk
FN1 high 56 55 52 51 50 49 45
FN1 low 69 66 61 54 51 46 43

◂**Fig. 7** Prognostic significance of autoantibodies against COL1A2, COL3A1, and FN1 in patients with DLBCL receiving R-CHOP ($n = 20$ and 125) and NSCLC treated with ICIs ($n = 36$). **A** Volcano plot, boxplot, and representative density plots of patients illustrating the distribution of COL1A2 autoantibodies in DLBCL. **B** Kaplan–Meier curve for PFS based on COL1A2 autoantibody levels in DLBCL. **C** Kaplan–Meier curves for OS and PFS in NSCLC patients receiving immunotherapy, stratified by COL1A2 and COL3A1 mRNA levels in GSE128989 and autoantibody presence, alongside representative density plots of COL1A2 and COL3A1 autoantibodies. **D** Comparison of FN1 autoantibody levels between healthy controls and DLBCL, with Kaplan–Meier analysis for PFS based on FN1 autoantibody levels. DLBCL: diffuse large B cell lymphoma; R-CHOP: rituximab, cyclophosphamide, doxorubicin: vincristine, and prednisone; NSCLC: non-small cell lung cancer; ICIs: immune checkpoint inhibitor; OS: overall survival; and PFS: progression-free survival

adenocarcinoma [45], breast cancer [46], gastric cancer [47], and thyroid cancer [48], *FN1* is positively correlated with higher macrophage infiltration. *SPP1*$^+$*FN1*$^+$ macrophages were first identified during the fibrosis process following cardiac and renal injury, showing expression of the resident macrophage marker gene *APOE*, and were demonstrated to have pro-fibrotic effects, capable of regulating fibroblast activation, also known as fibrogenic macrophages [49–52]. *SPP1*$^+$*FN1*$^+$ macrophages can alter the expression of inflammatory and fibrotic genes in fibroblasts via *FN1* [53]. In DLBCL, patients with higher expression of *FN1* were correlated with longer survival [13, 54–58], which aligns with our findings that FN1 levels at the mRNA and autoantibody levels were associated with favorable prognosis in DLBCL, and the colocalization of *FN1*$^+$ macrophages with *LYZ*$^+$ fibroblasts. *COL1A2* and *COL3A1* were fibrous collagens that encodes the precursor of the alpha 2 chain of type I collagen and alpha 1 chain of type III collagen [59]. *COL1A2* and *COL3A1* were highly expressed in smoking-related lung cancer [60], and *COL3A1* was upregulated in cisplatin-resistant lung cancer cells [61]. In lung adenocarcinoma, patients with high *COL3A1*-positive endothelial cell scores have better prognoses and lower metastatic risks, along with increased infiltration of cytotoxic cells (including macrophages, activated CD8-positive T cells, and NK cells), as well as the immune checkpoint molecules *CTLA-4*, *PDCD1*, and *PDCD1LG2* [62]. In melanoma, mutations in *COL3A1* were associated with improved overall survival in ICIs treatment, increased infiltration of pro-inflammatory M1 macrophages, and decreased infiltration of immunosuppressive M2 macrophages [63]. This aligns with our findings that COL3A1 levels at the mRNA and AAb levels were associated with favorable prognosis in NSCLC undergoing ICIs. COL1A2, as a regulatory factor for macrophages, was associated with higher levels of macrophage infiltration in various tumors (including melanoma [45], pancreatic ductal adenocarcinoma [46], colorectal cancer [47], and gastric cancer [48]). In DLBCL, *COL1A2* mRNA was expressed at lower levels in high-grade DLBCL compared to low-grade DLBCL [49], and it was positively correlated with favorable prognosis in DLBCL [7]. This aligns with our findings that COL1A2 levels at the mRNA and AAb levels were associated with favorable prognosis in DLBCL.

The identification of LYZ, FN1, COL1A2, and COL3A1 as robust prognostic biomarkers in both DLBCL and NSCLC opens new avenues for their clinical application. These biomarkers hold significant potential for integration into routine clinical practice, particularly for patient stratification, prediction of immunotherapy response, and monitoring of treatment efficacy. LYZ protein levels could serve as a valuable tool for identifying high-risk DLBCL and NSCLC patients, while elevated FN1 protein and autoantibody levels, along with COL3A1 protein expression, may predict improved responses to R-CHOP therapy in DLBCL. Furthermore, COL1A2 and COL3A1 autoantibodies could serve as predictive markers for response to ICIs therapy in NSCLC. By incorporating these biomarkers with existing prognostic tools, clinicians can refine risk assessment and tailor personalized treatment strategies, ultimately enhancing survival outcomes for DLBCL and NSCLC patients.

There are some limitations to this study. Firstly, while our approach identified *LYZ*$^+$ fibroblasts and *FN1*$^+$ macrophages, further functional studies are required to fully understand their biological roles within the TME in DLBCL. Second, our analysis did not explore the potential interactions between these fibroblast and macrophage subtypes and other immune cell populations, which may play critical roles in shaping the TME and influencing patient outcomes. Third, while we validated our findings in NSCLC samples, the generalizability of these results to other cancer types requires further investigation. Finally, in vivo and in vitro experiments are essential to confirm the therapeutic potential of the identified biomarkers and to evaluate their relevance across different cancers.

Conclusion

In summary, our study identified distinct *LYZ*$^+$ fibroblasts and *FN1*$^+$ macrophages within the TME of DLBCL, both of which demonstrated significant prognostic value and spatial colocalization. Key genes associated with these subtypes, including LYZ, LILRB4, COL1A2, and FN1, were correlated with improved patient survival in DLBCL and showed potential relevance in NSCLC. These findings suggest that these biomarkers may serve as promising candidates for further investigation into their therapeutic potential across cancer types. However, additional validation and functional studies are needed to confirm their roles and applicability in clinical settings.

Supplementary Information The online version contains supplementary material available at https://doi.org/10.1007/s00262-025-03968-7.

Acknowledgements Thanks to all the patients who participated in this study.

Author contributions Liyuan Dai contributed to conceptualization, data curation, methodology, formal analysis, investigation, validation, visualization, writing—original draft, and writing—review and editing, and provided software. Ning Lou was involved in resources, data curation, methodology, formal analysis, validation, and writing—review and editing. Liling Huang contributed to resources, data curation, methodology, formal analysis, validation, and writing—review and editing. Lin Li was involved in resources, data curation, investigation, and writing—review and editing. Le Tang contributed to resources, data curation, investigation, and writing—review and editing. Yuankai Shi was involved in conceptualization, funding acquisition, supervision, and writing—review and editing. Xiaohong Han contributed to conceptualization, funding acquisition, supervision, and writing—review and editing.

Funding This work was supported by the Beijing Natural Science Foundation (7252207), National High Level Hospital Clinical Research Funding (2022-PUMCH-B-033), CAMS Innovation Fund for Medical Sciences under Grant (CIFMS 2021-I2M-1–003), and the Major Project of Medical Oncology Key Foundation of Cancer Hospital Chinese Academy of Medical Sciences (CICAMS-MOMP2022006).

Data availability The datasets used and/or analyzed during the current study are available from the corresponding author on reasonable request. The accession number for the raw sequencing data deposited in Genome Sequence Archive (GSA) is HRA006757. Details of the spatial transcriptomics data can be found at https://ngdc.cncb.ac.cn/gsa-human/browse/HRA006757.

Declarations

Conflict of interests The authors report there are no competing interests to declare. All authors agreed to submit for consideration for publication in this journal.

Ethical approval and consent to participate This study has been approved by the Ethics Committee of the National Cancer Center/National Clinical Research Center for Cancer/Cancer Hospital, Chinese Academy of Medical Sciences & Peking Union Medical College (No. 23/262-4004 and No.22/486-3688). All experiments were executed according to the Declaration of Helsinki.

Consent for publication All authors agreed to submit for consideration for publication in this journal.

References

1. Evans LS, Hancock BW (2003) Non-Hodgkin lymphoma. The Lancet 362:139–146. https://doi.org/10.1016/s0140-6736(03)13868-8
2. Sehn LH, Salles G (2021) Diffuse large B-cell lymphoma. N Engl J Med 384:842–858. https://doi.org/10.1056/NEJMra2027612
3. Ruppert AS, Dixon JG, Salles G et al (2020) International prognostic indices in diffuse large B-cell lymphoma: a comparison of IPI, R-IPI, and NCCN-IPI. Blood 135:2041–2048. https://doi.org/10.1182/blood.2019002729
4. Chen F, Zhuang X, Lin L et al (2015) New horizons in tumor microenvironment biology: challenges and opportunities. BMC Med 13:45. https://doi.org/10.1186/s12916-015-0278-7
5. Liu Y, Zhou X, Wang X (2021) Targeting the tumor microenvironment in B-cell lymphoma: challenges and opportunities. J Hematol Oncol 14:125. https://doi.org/10.1186/s13045-021-01134-x
6. Desbois M, Wang Y (2021) Cancer-associated fibroblasts: key players in shaping the tumor immune microenvironment. Immunol Rev 302:241–258. https://doi.org/10.1111/imr.12982
7. Ansell SM, Minnema MC, Johnson P et al (2019) Nivolumab for relapsed/refractory diffuse large B-cell lymphoma in patients ineligible for or having failed autologous transplantation: a single-arm, phase II study. J Clin Oncol 37:481–489. https://doi.org/10.1200/jco.18.00766
8. Schuster SJ, Bishop MR, Tam CS et al (2019) Tisagenlecleucel in adult relapsed or refractory diffuse large B-cell lymphoma. N Engl J Med 380:45–56. https://doi.org/10.1056/NEJMoa1804980
9. Augsten M (2014) Cancer-associated fibroblasts as another polarized cell type of the tumor microenvironment. Front Oncol 4:62. https://doi.org/10.3389/fonc.2014.00062
10. Tsoumakidou M (2023) The advent of immune stimulating CAFs in cancer. Nat Rev Cancer 23:258–269. https://doi.org/10.1038/s41568-023-00549-7
11. Kotlov N, Bagaev A, Revuelta MV et al (2021) Clinical and biological subtypes of B-cell lymphoma revealed by microenvironmental signatures. Cancer Discov 11:1468–1489. https://doi.org/10.1158/2159-8290.Cd-20-0839
12. Steen CB, Luca BA, Esfahani MS et al (2021) The landscape of tumor cell states and ecosystems in diffuse large B cell lymphoma. Cancer Cell 39:1422-1437.e1410. https://doi.org/10.1016/j.ccell.2021.08.011
13. Ciavarella S, Vegliante MC, Fabbri M et al (2018) Dissection of DLBCL microenvironment provides a gene expression-based predictor of survival applicable to formalin-fixed paraffin-embedded tissue. Ann Oncol 29:2363–2370. https://doi.org/10.1093/annonc/mdy450
14. Staiger AM, Duppel J, Dengler MA et al (2017) An analysis of the role of follicular lymphoma-associated fibroblasts to promote tumor cell viability following drug-induced apoptosis. Leuk Lymphoma 58:1922–1930. https://doi.org/10.1080/10428194.2016.1263841
15. Bankov K, Döring C, Ustaszewski A et al (2019) Fibroblasts in nodular sclerosing classical hodgkin lymphoma are defined by a specific phenotype and protect tumor cells from

brentuximab-vedotin induced injury. Cancers. https://doi.org/10.3390/cancers11111687

16. Dai L, Fan G, Xie T et al (2024) Single-cell and spatial transcriptomics reveal a high glycolysis B cell and tumor-associated macrophages cluster correlated with poor prognosis and exhausted immune microenvironment in diffuse large B-cell lymphoma. Biomark Res 12:58. https://doi.org/10.1186/s40364-024-00605-w
17. Visco C, Li Y, Xu-Monette ZY et al (2012) Comprehensive gene expression profiling and immunohistochemical studies support application of immunophenotypic algorithm for molecular subtype classification in diffuse large B-cell lymphoma: a report from the International DLBCL Rituximab-CHOP Consortium Program Study. Leukemia 26:2103–2113. https://doi.org/10.1038/leu.2012.83
18. Barrans SL, Crouch S, Care MA et al (2012) Whole genome expression profiling based on paraffin embedded tissue can be used to classify diffuse large B-cell lymphoma and predict clinical outcome. Br J Haematol 159:441–453. https://doi.org/10.1111/bjh.12045
19. Dubois S, Tesson B, Mareschal S et al (2019) Refining diffuse large B-cell lymphoma subgroups using integrated analysis of molecular profiles. EBioMedicine 48:58–69. https://doi.org/10.1016/j.ebiom.2019.09.034
20. Dai L, Chen H, Tan Q et al (2024) Identification of novel prognostic autoantibodies in diffuse large B-cell lymphoma treated with rituximab plus cyclophosphamide, doxorubicin, vincristine, and prednisone via a high-throughput antigen microarray. Cancer 130:1257–1269. https://doi.org/10.1002/cncr.35158
21. Lou N, Wang G, Wang Y et al (2023) Proteomics identifies circulating TIMP-1 as a prognostic biomarker for diffuse large B-cell lymphoma. Mol Cell Proteomics 22:100625. https://doi.org/10.1016/j.mcpro.2023.100625
22. Dai L, Tan Q, Li L et al (2024) High-throughput antigen microarray identifies longitudinal prognostic autoantibody for chemoimmunotherapy in advanced non-small cell lung cancer. Mol Cell Proteomics 23:100749. https://doi.org/10.1016/j.mcpro.2024.100749
23. Apollonio B, Spada F, Petrov N et al (2023) Tumor-activated lymph node fibroblasts suppress T cell function in diffuse large B cell lymphoma. J Clin Invest. https://doi.org/10.1172/jci166070
24. Nan YY, Zhang WJ, Huang DH et al (2021) Evaluation of a five-gene signature associated with stromal infiltration for diffuse large B-cell lymphoma. World J Clin Cases 9:4585–4598. https://doi.org/10.12998/wjcc.v9.i18.4585
25. Haro M, Orsulic S (2018) A paradoxical correlation of cancer-associated fibroblasts with survival outcomes in B-cell lymphomas and carcinomas. Front Cell Dev Biol 6:98. https://doi.org/10.3389/fcell.2018.00098
26. Franquesa M, Mensah FK, Huizinga R et al (2015) Human adipose tissue-derived mesenchymal stem cells abrogate plasmablast formation and induce regulatory B cells independently of T helper cells. Stem Cells 33:880–891. https://doi.org/10.1002/stem.1881
27. Liu J, Wang N, Liu Y et al (2018) The antimicrobial spectrum of lysozyme broadened by reductive modification. Poult Sci 97:3992–3999. https://doi.org/10.3382/ps/pey245
28. Lee W, Ku SK, Na DH et al (2015) Anti-inflammatory effects of lysozyme against HMGB1 in human endothelial cells and in mice. Inflammation 38:1911–1924. https://doi.org/10.1007/s10753-015-0171-8
29. Bergamo A, Gerdol M, Pallavicini A et al (2019) Lysozyme-induced transcriptional regulation of TNF-α pathway genes in cells of the monocyte lineage. Int J Mol Sci. https://doi.org/10.3390/ijms20215502
30. Ren Y, Yu M, Zheng D et al (2024) Lysozyme promotes renal fibrosis through the JAK/STAT3 signal pathway in diabetic nephropathy. Arch Med Sci 20:233–247. https://doi.org/10.5114/aoms/170160
31. Zhou YJ, Lu XF, Chen H et al (2023) Single-cell transcriptomics reveals early molecular and immune alterations underlying the serrated neoplasia pathway toward colorectal cancer. Cell Mol Gastroenterol Hepatol 15:393–424. https://doi.org/10.1016/j.jcmgh.2022.10.001
32. Xiong D, Wei X, Huang W et al (2024) Prediction significance of autophagy-related genes in survival probability and drug resistance in diffuse large B-cell lymphoma. Aging 16:1049–1076. https://doi.org/10.18632/aging.205282
33. Shi H, Pan Y, Xiang G et al (2023) A novel NET-related gene signature for predicting DLBCL prognosis. J Transl Med 21:630. https://doi.org/10.1186/s12967-023-04494-9
34. Jiang Y, Sun H, Xu H et al (2022) Immunophenotypic landscape and prognosis-related mRNA signature in diffuse large B cell lymphoma. Front Genet 13:872001. https://doi.org/10.3389/fgene.2022.872001
35. Barros MH, Segges P, Vera-Lozada G et al (2015) Macrophage polarization reflects T cell composition of tumor microenvironment in pediatric classical Hodgkin lymphoma and has impact on survival. PLoS ONE 10:e0124531. https://doi.org/10.1371/journal.pone.0124531
36. Guo TK, Zhao X, Xie XD et al (2007) The anti-proliferative effects of recombinant human lysozyme on human gastric cancer cells. J Int Med Res 35:353–360. https://doi.org/10.1177/147323000703500310
37. Choi JI, Cho EJ, Yang MJ et al (2023) Hypoxic microenvironment determines the phenotypic plasticity and spatial distribution of cancer-associated fibroblasts. Clin Transl Med 13:e1438. https://doi.org/10.1002/ctm2.1438
38. Chakraborty D, Šumová B, Mallano T et al (2017) Activation of STAT3 integrates common profibrotic pathways to promote fibroblast activation and tissue fibrosis. Nat Commun 8:1130. https://doi.org/10.1038/s41467-017-01236-6
39. Chang SS, Cheng CC, Chen YR et al (2024) Epithelial CEBPD activates fibronectin and enhances macrophage adhesion in renal ischemia-reperfusion injury. Cell Death Discov 10:328. https://doi.org/10.1038/s41420-024-02082-4
40. Huleihel L, Dziki JL, Bartolacci JG et al (2017) Macrophage phenotype in response to ECM bioscaffolds. Semin Immunol 29:2–13. https://doi.org/10.1016/j.smim.2017.04.004
41. Li M, Wang K, Pang Y et al (2020) Secreted phosphoprotein 1 (SPP1) and fibronectin 1 (FN1) are associated with progression and prognosis of esophageal cancer as identified by integrated expression profiles analysis. Med Sci Monit 26:e920355. https://doi.org/10.12659/msm.920355
42. Jiang K, Liu H, Xie D et al (2019) Differentially expressed genes ASPN, COL1A1, FN1, VCAN and MUC5AC are potential prognostic biomarkers for gastric cancer. Oncol Lett 17:3191–3202. https://doi.org/10.3892/ol.2019.9952
43. Zhou WH, Du WD, Li YF et al (2022) The overexpression of fibronectin 1 promotes cancer progression and associated with M2 macrophages polarization in head and neck squamous cell carcinoma patients. Int J Gen Med 15:5027–5042. https://doi.org/10.2147/ijgm.S364708
44. Zhang L, Zhang C, Xing Z et al (2022) Fibronectin 1 derived from tumor-associated macrophages and fibroblasts promotes metastasis through the JUN pathway in hepatocellular carcinoma. Int Immunopharmacol 113:109420. https://doi.org/10.1016/j.intimp.2022.109420
45. Xavier CPR, Castro I, Caires HR et al (2021) Chitinase 3-like-1 and fibronectin in the cargo of extracellular vesicles shed by

human macrophages influence pancreatic cancer cellular response to gemcitabine. Cancer Lett 501:210–223. https://doi.org/10.1016/j.canlet.2020.11.013

46. Wu L, Zhou Y, Guan Y et al (2021) Seven genes associated with lymphatic metastasis in thyroid cancer that is linked to tumor immune cell infiltration. Front Oncol 11:756246. https://doi.org/10.3389/fonc.2021.756246
47. Sullivan KM, Li H, Yang A et al (2024) Tumor and peritoneum-associated macrophage gene signature as a novel molecular biomarker in gastric cancer. Int J Mol Sci. https://doi.org/10.3390/ijms25074117
48. Wang H, Zhang J, Li H et al (2022) FN1 is a prognostic biomarker and correlated with immune infiltrates in gastric cancers. Front Oncol 12:918719. https://doi.org/10.3389/fonc.2022.918719
49. Hoeft K, Schaefer GJL, Kim H et al (2023) Platelet-instructed SPP1(+) macrophages drive myofibroblast activation in fibrosis in a CXCL4-dependent manner. Cell Rep 42:112131. https://doi.org/10.1016/j.celrep.2023.112131
50. Ouyang Q, Wang C, Sang T et al (2024) Depleting profibrotic macrophages using bioactivated in vivo assembly peptides ameliorates kidney fibrosis. Cell Mol Immunol 21:826–841. https://doi.org/10.1038/s41423-024-01190-6
51. Qi J, Sun H, Zhang Y et al (2022) Single-cell and spatial analysis reveal interaction of FAP(+) fibroblasts and SPP1(+) macrophages in colorectal cancer. Nat Commun 13:1742. https://doi.org/10.1038/s41467-022-29366-6
52. Fabre T, Barron AMS, Christensen SM et al (2023) Identification of a broadly fibrogenic macrophage subset induced by type 3 inflammation. Sci Immunol. https://doi.org/10.1126/sciimmunol.add8945
53. Nakamura R, Bing R, Gartling GJ et al (2022) Macrophages alter inflammatory and fibrotic gene expression in human vocal fold fibroblasts. Exp Cell Res 419:113301. https://doi.org/10.1016/j.yexcr.2022.113301
54. Lossos IS, Czerwinski DK, Alizadeh AA et al (2004) Prediction of survival in diffuse large-B-cell lymphoma based on the expression of six genes. N Engl J Med 350:1828–1837. https://doi.org/10.1056/NEJMoa032520
55. Lenz G, Wright G, Dave SS et al (2008) Stromal gene signatures in large-B-cell lymphomas. N Engl J Med 359:2313–2323. https://doi.org/10.1056/NEJMoa0802885
56. Brandt S, Montagna C, Georgis A et al (2013) The combined expression of the stromal markers fibronectin and SPARC improves the prediction of survival in diffuse large B-cell lymphoma. Exp Hematol Oncol 2:27. https://doi.org/10.1186/2162-3619-2-27
57. Tekin N, Omidvar N, Morris TP et al (2016) Protocol for qRT-PCR analysis from formalin fixed paraffin embedded tissue sections from diffuse large b-cell lymphoma: validation of the six-gene predictor score. Oncotarget 7:83319–83329. https://doi.org/10.18632/oncotarget.13066
58. Gao Y, Sun B, Hu J et al (2020) Identification of gene modules associated with survival of diffuse large B-cell lymphoma treated with CHOP-based chemotherapy. Pharmacogenomics J 20:705–716. https://doi.org/10.1038/s41397-020-0161-6
59. Kuivaniemi H, Tromp G (2019) Type III collagen (COL3A1): gene and protein structure, tissue distribution, and associated diseases. Gene 707:151–171. https://doi.org/10.1016/j.gene.2019.05.003
60. Chen Y, Pan Y, Ji Y et al (2018) Network analysis of differentially expressed smoking-associated mRNAs, lncRNAs and miRNAs reveals key regulators in smoking-associated lung cancer. Exp Ther Med 16:4991–5002. https://doi.org/10.3892/etm.2018.6891
61. Wang L, Sun Y, Guo Z et al (2022) COL3A1 overexpression associates with poor prognosis and cisplatin resistance in lung cancer. Balkan Med J 39:393–400. https://doi.org/10.4274/balkanmedj.galenos.2022.2022-6-16
62. Zhang M, Liang Y, Song P (2024) COL3A1-positive endothelial cells influence LUAD prognosis and regulate LUAD carcinogenesis by NCL-PI3K-AKT axis. J Gene Med. https://doi.org/10.1002/jgm.3573
63. Zhang W, Kong Y, Li Y et al (2021) Novel molecular determinants of response or resistance to immune checkpoint inhibitor therapies in melanoma. Front Immunol 12:798474. https://doi.org/10.3389/fimmu.2021.798474

Authors and Affiliations

Liyuan Dai[1] · Ning Lou[1,3] · Liling Huang[1] · Lin Li[2] · Le Tang[1] · Yuankai Shi[1] · Xiaohong Han[3]

✉ Yuankai Shi
syuankai@cicams.ac.cn

✉ Xiaohong Han
hanxiaohong@pumch.cn

[1] Department of Medical Oncology, National Cancer Center/National Clinical Research Center for Cancer/Cancer Hospital, Chinese Academy of Medical Sciences & Peking Union Medical College, No. 17 Panjiayuan Nanli, Chaoyang District, Beijing 100021, China

[2] Department of Pathology, National Cancer Center/National Clinical Research Center for Cancer/Cancer Hospital, Chinese Academy of Medical Sciences & Peking Union Medical College, No. 17 Panjiayuan Nanli, Chaoyang District, Beijing 100021, China

[3] Clinical Pharmacology Research Center, Peking Union Medical College Hospital, State Key Laboratory of Complex Severe and Rare Diseases, NMPA Key Laboratory for Clinical Research and Evaluation of Drug, Beijing Key Laboratory of Clinical PK & PD Investigation for Innovative Drugs, Chinese Academy of Medical Sciences & Peking Union Medical College, No.1, Shuaifuyuan, Dongcheng District, Beijing 100730, China